Available online at www.sciencedirect.com

ScienceDirect

Journal of Magnesium and Alloys 12 (2024) 1511–1517

www.elsevier.com/locate/jma

Letter

Anomalous $\{10\bar{1}2\}$ tensile twinning and subsequent detwinning in a friction stir processed carbon fiber-reinforced Mg composite

1. Main text

Owing to their low density and high specific strength, magnesium alloys and magnesium-based composites have great potential as structure metal materials in applications where lightweight matters [1–4]. Deformation twins [5], especially the $\{10\bar{1}2\}$ tension twins (also called tensile or extension twins) with a low critical resolved shear stress (CRSS) [6], are commonly observed in Mg alloys. They can provide the much-needed deformation along the c-axis in their hcp structure resulting from the very few easily activated ⟨a⟩ slip systems in this crystal structure [7]. The tensile twinning activation usually follows the macroscopic Schmid factor law [2], i.e., the twin variant with the highest Schmid factor occurs, and it only appears when its Schmid factor is positive.

However, some postmortem microstructure studies show that these tensile twins did appear without obeying the Schmid criterion [8–18], even when their macro-Schmid factor is negative [9,10,14,17]. These postmortem observations of the anomalous tension twins are attributed to unloading or local anomalous stress states [17], or as a consequence of strain accommodation to compensate for the strain from basal slip activity [19]. Very recently, an *in-situ* electron backscatter diffraction (EBSD) compression study (which can provide both local and global strain information while other postmortem studies cannot) of Mg-rare-earth alloys also reported that many activated tensile twins do not obey the Schmid law. This study confirms that sometimes location stress/strain conditions play a more important role than the globally applied stress [20].

The observation mentioned above of anomalous tension twinning is either based on the postmortem microstructure or low-strain *in-situ* studies. However, no subsequent detwinning of these anomalous tension twins has been reported. This detwinning is possible. For example, anomalous tension twins can form at a low strain due to the local stress condition (which is different from the macroscopically applied stress). As the deformation proceeds, its location stress changes and then becomes similar to the applied stress in its direction. This change in stress direction will shrink the highly mobile tension twin boundary and then possibly make it disappear. This process is highly similar to the well-known detwinning process in Mg alloys or Mg-based composite during unloading or reverse-loading [21–32]. In the present study, we confirm the proposed hypothesis and observe the whole process – the anomalous twinning at a low strain and, importantly, the (complete) detwinning of these anomalous twins at a higher strain with *in-situ* tensile EBSD technique for a model carbon fiber reinforced Mg composite (Mg-CF). This model material was prepared by a refill friction stir welding method [30], as shown in Supplementary Fig. S1a. The tensile specimens contain 10.5 vt.% carbon fibers with a gradient distribution in thickness dimension.

The commercial pure Mg sheets with a thickness of 1 mm were utilized, and the carbon fiber (CF) with a diameter of 6.9μm was placed between the pure Mg sheets. Before welding, the pure Mg sheets were mechanical grinding and polished to remove the oxide layer. The welding was conducting on an RFSSW machine with the excution parameter setting as (1) the rotation speed of 1600 RPM; (2) the penetration depths of 1 mm; (3) the penetration speed of 1 mm/s and (4) the reaction speed of 2 mm/s. The distribution of carbon fiber was characterized by a dual beam electron microscope (Thermofisher Scios 2, FIB) using the fracture of the deformed sample. A dog-bone tensile specimen with gauge dimensions of 2 mm × 1 mm × 1.5 mm was cut by spark machining. The gauge section is located in the welding nut (See Supplementary Fig. S1b) and as close to the center as possible. A schematic (Fig. 1) is drawn to depict the welding process and sampling method. The specimen surface was then mechanically ground and electrolytically polished to a mirror level, which is critical to obtaining the high-quality EBSD pattern. A tensile tester was used to deform the specimen in an FEI Nova NanoSEM 430 scanning electron microscope coupled with an EBSD system (Oxford Nordlys EBSD detector). Dual threaded leadscrews ensure that the center of the specimen stays centrally located during tension. The tensile sample was deformed at a displacement rate of around 1 μm/s to a displacement of 100 μm, 200 μm, 300 μm, 380 μm, 500 μm and cracking conditions (560 μm) to allow electron backscatter diffraction pattern collection. At each interrupted step, automated beam mapping contained a 100 × 200 μm^2 area with a 0.5 μm step size. It should be noted that the surface used to collect the EBSD pattern is the side parallel to

https://doi.org/10.1016/j.jma.2023.10.008
2213-9567/© 2023 Chongqing University. Publishing services provided by Elsevier B.V. on behalf of KeAi Communications Co. Ltd. This is an open access article under the CC BY-NC-ND license (http://creativecommons.org/licenses/by-nc-nd/4.0/) Peer review under responsibility of Chongqing University

the tensile direction, and the collection area is located on the Mg matrix. The processing and analysis of EBSD data were achieved by Channel 5 and MTEX. Separated tensile tests of the Mg-CF samples were conducted using a universal testing machine (KAIPLE-P5) with a video extensometer measuring system at the same strain rate ($2 \times 10^{-3}\ s^{-1}$). This is to obtain an engineering stress–strain curve for the sample. The obtained engineering stress–strain curve and the engineering stress–displacement curve from the *in-situ* EBSD can then be correlated. This correlation can provide a rough estimation of the engineering strain for each interrupted EBSD scan from the *in-situ* test's engineering stress.

As shown in Fig. 2a, a SEM image of the fracture was utilized to present the distribution of CF in the sample. The magnified images corresponding to the three different colored selection areas in Fig. 2a clearly show the content of CF in the respective regions (pointed by white arrows), where the volume fraction of CF ranges from 3% to 22% based on the statistics of numerous fracture morphology at different thickness dimension. This indicates that a density gradient distribution exists along the thickness direction of the sample (see Fig. 2b-d). Such gradient distribution of reinforcement is ascribed to the welding process and sampling method. A representative EBSD mapping of the undeformed sample is presented in Fig. 2e. All of the EBSD inverse pole figure (IPF) mapping shown in this paper are colored according to the horizontal axis-Y, which is perpendicular to the tensile direction.

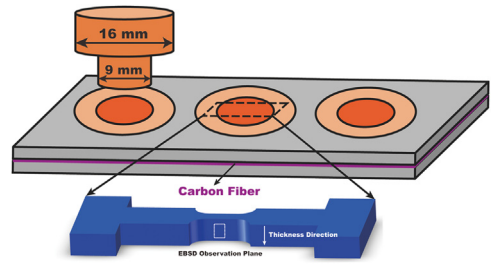

Fig. 1. The schematic of welding process and sampled *in-situ* tensile specimen with testing plane.

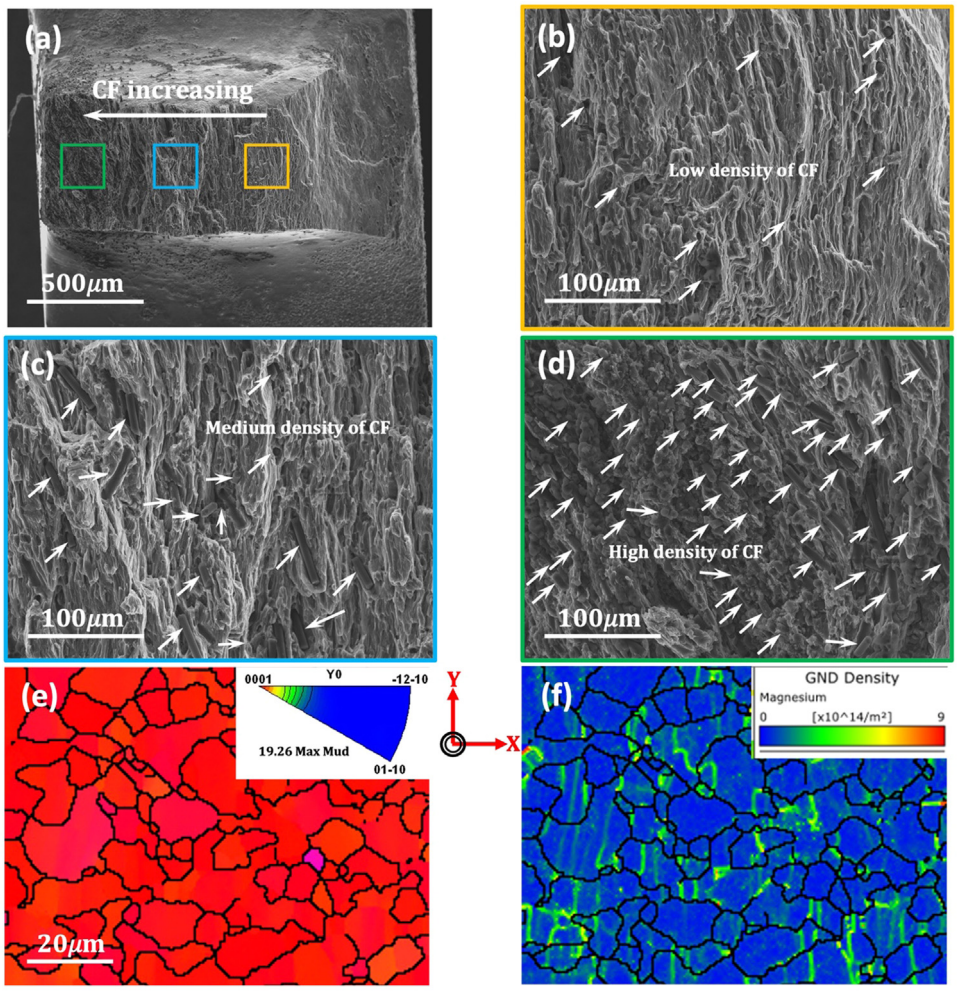

Fig. 2. (a) SEM image of fractured Mg-CFs composite showing the distribution of carbon fibers. (b-d) The enlarged images corresponding to the three squared selections in (a) with different color. (e) Representative EBSD mapping of the undeformed sample with IPF coloring parallel Y-axis. (f) The geometrical necessary dislocation (GND) mapping corresponding to (e). (For interpretation of the references to colour in this figure legend, the reader is referred to the web version of this article.)

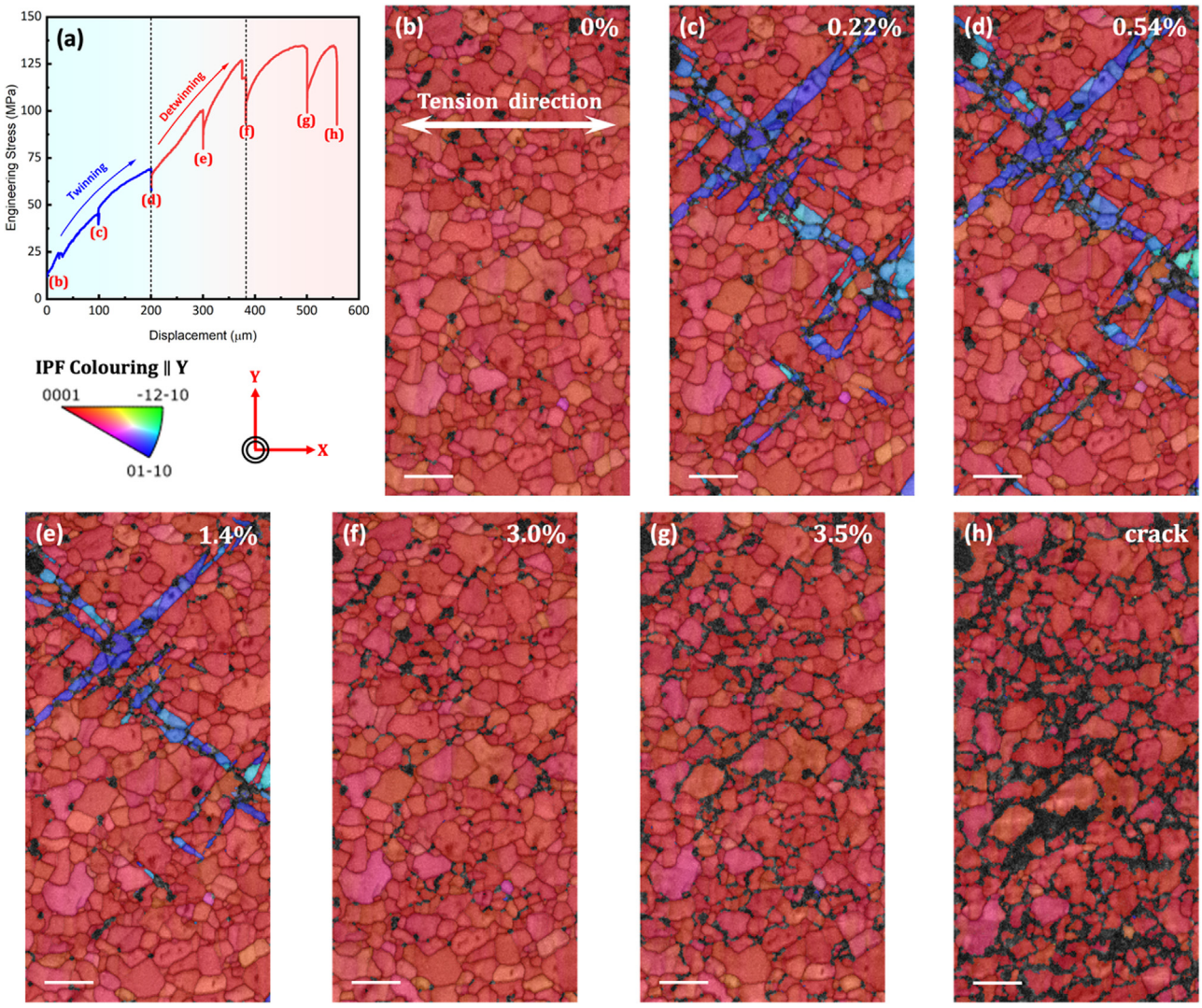

Fig. 3. (a) Engineering stress-displacement curve for the *in-situ* tensile test. (b-h) The inverse pole figure maps (with respect to the Y-axis) superimposed on the band contrast map at a strain of 0%, 0.22%, 0.54%, 1.42%, 3.0%, 3.5%, and cracking. The microbar is 20 μm.

This is to obtain a more noticeable color contrast, facilitating the analysis of deformation twinning in the following part. The used Mg-CF composites have an average grain size of 9 μm. An extremely strong ⟨0001⟩ texture along the Y-axis was demonstrated by inverse pole figure (IPF) with a maximum multiple of uniform density (mud) of 19.26. The corresponding Kernel average misorientation (KAM) mapping (Fig. 2f) exhibits a high level of geometrically necessary dislocations (GND) (in the order of $10^{14}m^{-2}$), which may result from the residual thermal stress during the fabricating process.

Fig. 3a shows the engineering stress-displacement curve of the *in-situ* tensile test. Its corresponding IPF mappings under different displacements are illustrated in Fig. 3b-h. It should be mentioned that a typical engineering stress–strain curve of the Mg-CF sample in the same condition is also shown in Supplementary Fig. S2. Therefore, we can roughly estimate the following strains for all the interrupted displacements of the *in-situ* tensile test: which are 0.22%, 0.54%, 1.4%, 3.0%, and 3.5% for the corresponding displacements of 100 μm (45 MPa), 200 μm (69 MPa), 300 (100 MPa) μm, 380 μm (127 MPa), and 500 μm (134 MPa), respectively. For consistency, the estimated strain values will be utilized as state parameters in the subsequent descriptions.

The undeformed state in Fig. 3b exhibits a clean microstructure without pre-existing twin boundaries. Twinning occurred in the collection area when the tensile specimen was deformed to a strain of 0.22%. These twins were identified as $\{10\bar{1}2\}$ $<10\bar{1}1>$ - extension twins with a misorientation of 86° $<11\bar{2}0>$ to the parent grains. The occurrence of twinning is also reflected in the stress-displacement curve. At the stress of about 25 MPa, a distinct stress fluctuation is captured, generally taken as a sign of twinning propagation [2,33,34]. It should be pointed out that due to the strong texture of the matrix, the orientation differences between neighboring grains are small (specifically, most of the large angle grain boundaries in the collection area are distributed at 15°−30°, as shown in Supplementary Fig. S3), which renders the behavior of twinning transmission extremely active [35]. This

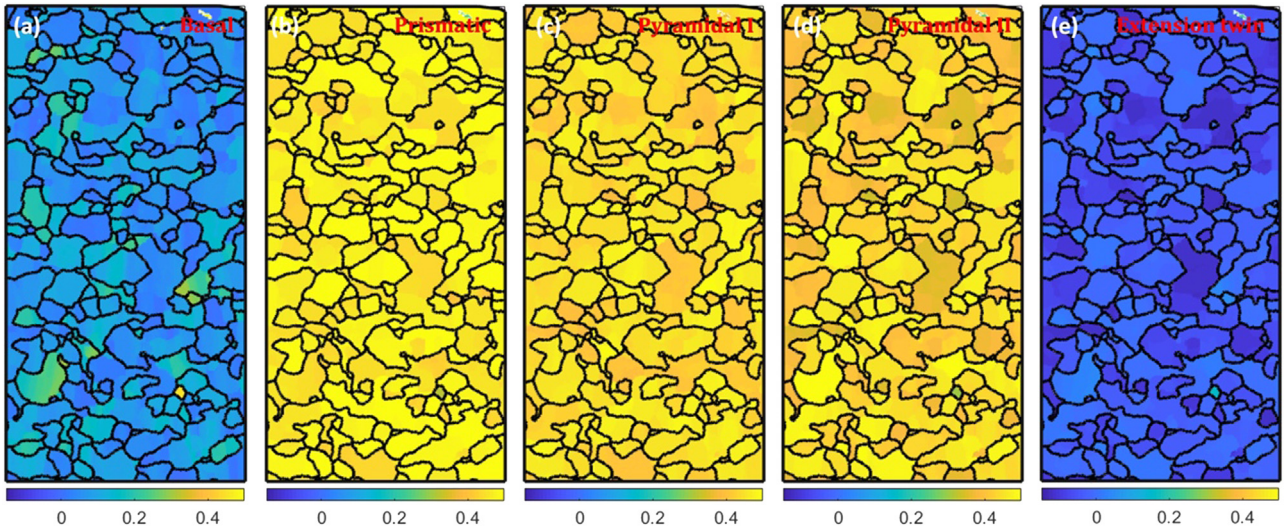

Fig. 4. (a-e) The maximum Schmid factor mappings of basal slip, prismatic slip, pyramidal I slip, pyramidal II slip, and extension twin, corresponding to the undeformed state.

phenomenon, called the twin cascade effect, makes the fluctuation more evident on the stress-displacement curve [33–35]. As the strain increases to 0.54%, twinning is still increasing but at a significantly slower rate (the twin area only from 16.6% to 17.1%) (see Supplementary Fig. S4). When the displacement reaches 1.42%, as shown in Fig. 3e, the twinning area proportion decreases from 17.1% to 9.7% (Fig. S4). The disappearance of the scattered twins and the reduction of the twin thickness in the high-density twinning area are responsible for the decrease in proportion. Surprisingly, as the strain increases to 3.0%, the previously existing high-density twinning region completely disappears, which means that the deformation twins generated before the strain of 0.54% are entirely de-twinned. And until the fracture, no new deformation twins occur.

Thus far, to the best of our knowledge, we observed a novel phenomenon that has never been reported in the literature – the Mg matrix undergoes twinning and detwinning successively in the tensile loading process. To understand this phenomenon, we need to answer two questions: i) how are deformation twins formed? ii) why does detwinning occur?

As mentioned above, the type of deformation twins is $\{10\bar{1}2\}$ extension twins. As a crucial deformation mechanism compensating for strain out of the basal plane, it induces an extension along the c-axis [7]. $\{10\bar{1}2\}$ extension twins typically obey the Schmid criterion, i.e., the twin variants with the highest Schmid factor are activated first in a fashion similar to slip [36]. Moreover, the *in-situ* EBSD results show that grains do not undergo drastic changes in orientation except for specific orientation changes caused by twinning during deformation. Therefore, it is reasonable to conjecture the potential for the deformation mechanism to occur based on the orientation information of the undeformed state. Fig. 4a-e show the corresponding mappings of the maximum Schmid factor for five prevalent deformation mechanisms, including basal slip, prismatic slip, pyramidal I slip, pyramidal II slip, and $\{10\bar{1}2\}$ extension twinning in the undeformed state. The maximum macroscopic Schmid factors of prismatic slip, pyramidal I slip, and pyramidal II slip are all distributed above 0.4, while those of basal slip and extension twin are significantly lower. Especially, the maximum Schmid factors of extension twinning are negative or approaching zero for almost all regions in the observation area. This result suggests that the extension twins ought not to form at all based on the macroscopic stress state since extension twinning cannot operate in the case of contraction along the c-axis or in the case that the shear stress along the twinning direction approaches zero. Therefore, back to the first question, how does this anomalous twinning occur?

As illustrated in [12], Molodov et al. reported that anomalous twinning plays a role in coordinating local strain during the plastic deformation of Mg. Thanks to the *in-situ* EBSD tensile test, localmicroscopic strain and macroscopic tensile strain can be combined to facilitate the analysis. Three lines parallel to the tensile direction were plotted on the EBSD mapping to track the evolution of distance between two randomly selected grains, as shown in Fig. 5a-c. The two end points of these three lines are chosen carefully in such a way that they are always in the same featured locations of the selected grain boundary position based on the band contrast map. And we only pay attention to the relative length change in the loading direction. The information that the variation in the length of the three lines corresponding to different tensile strains was utilized to calculate the micro-strain of the data collection area. Here, the micro-strain along the loading direction is simply interpreted as the rate of variation in liner length for different macro-strains. Fig. 5d displays the evolution of micro-strain as macro-strain increases. The three lines all exhibit a first descending and then an ascending trend. An abnormal result is that the micro-strain shows a negative value in the early stage of deformation. This signifies that the Mg matrix withstands a compressive strain, which is contrary

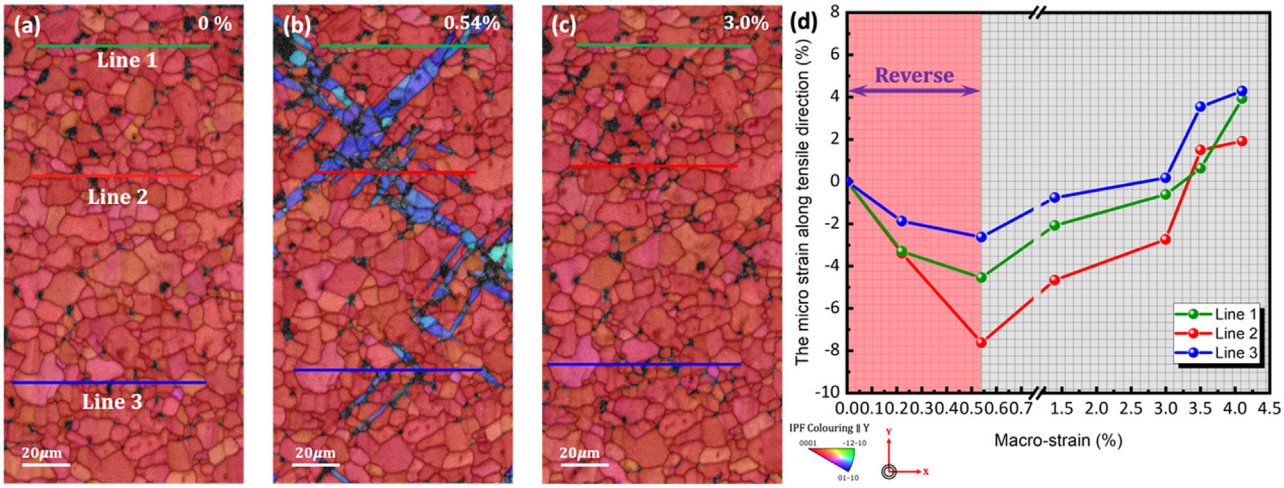

Fig. 5. (a-c) Lengths of three-line segments parallel to the tensile direction at a strain of 0%, 0.54% and 3.0%. These lines were used to measure the distance variations between two grains at different macro-strain. (d) The evolution of micro-strain along the tensile direction as the marco-strain increases.

to the macroscopic tensile strain. It should be noted that the red line (Line 2) crossing the main twinning region exhibits a more substantial contradiction to the macroscopic strain than the other two lines. This suggests that the appearance of the twinned area is due to more intense compressive strain than the un-twinned area. The micro-strain exhibiting a reverse trend to the macroscopic strain was derived from the strain compatibility between the Mg matrix and CFs. Due to the large strength disparity between matrix and CFs, the matrix was first subjected to plastic deformation while the CFs were still in elastic deformation in the early stage of the tensile test. The inherently high density of geometrically necessary dislocations further contributes to a state of compressive stress in the Mg matrix. It thus ensures a synergistic deformation of the materials as a whole. The gradient distribution of the carbon fiber along the thickness direction may also contribute to the micro-strain trends seen in Fig. 5d, which will be discussed in more detail later.

Based on this result, the maximum Schmid factor distribution of extension twinning corresponding to the undeformed state under compressive stress is shown in Fig. 6a. A high value of Schmid factor excessing 0.4 was widely distributed in the collection area. Two typical twinned grains are selected to recalculate their Schmid factor under compressive load. Fig. 6c and d illustrate the calculated possible slip plane traces of six twin variants of each grain, annotated with the corresponding Schmid factor. By matching with the observed slip plane trace (solid red line), it can be found that the actual twin variants generated during deformation both have the highest Schmid factor, in line with the mentioned Schmid criterion. It should be noted that the Schmid factor of various slips does not change whether under tension or compression applied stress since they do not have a polar feature like deformation twinning [5]. Although the pyramidal slip mechanism and prismatic slipping mechanism are also favored with the texture of the Mg matrix, they require a significantly higher CRSS to activate than extension twinning [2,37,38]. Therefore, extension twinning can stand out from the competition with other dislocation mechanisms.

The relationship between micro-strain and macro-strain also determines the occurrence of detwinning. After a tensile strain of 0.54%, the changing trend of the micro-strain is consistent with the macrostrain, which indicates the stress state of the Mg matrix starts to change from compressive stress to tensile stress. Unlike the pinning effect of some solute atoms on twin boundaries in Mg alloy [30], the detwinning in pure Mg will occur more readily once the stress state activating twins is not satisfied. The tensile strain of 0.54%, as the inflection point of micro-strain evolution, confirms the phenomenon that detwinning occurs after this macro-strain. Furthermore, when the micro-strain converts from compressive strain to tensile strain, as shown by the maximum Schmid factor distribution calculated in Fig. 4e, matrix orientation is no longer favorable for $\{10\bar{1}2\}$ extension twinning.

The current study confirms that the local stress/strain state plays a key role in activating anomalous twin. It is worth noting that two factors might contribute to the observed local compressive stress state at the start of the tensile loading. One is the compressive residual stress in the matrix after cooling, as evidenced by the high density of GND existing in the undeformed state (Fig. 2f). The state of compressive residual stress in the Mg matrix can be attributed to the non-uniform distribution of carbon fiber along with a large thermal mismatch between the carbon fiber and pure Mg. the thermal expansion coefficient of carbon fiber and pure Mg is -1.14 $\times$ 10^{-6} K^{-1} and 26 $\times$ 10^{-6} K^{-1} [39], respectively. This significant difference in the thermal expansion coefficient generates a large thermal mismatch between the matrix and reinforcing phase, which leads to compressive residual stress in the matrix. Similar results where the matrix suffered compressive residual stress were also have been reported in Al-graphene prepared by friction stir welding [40,41]. The other is the 'plastically non-homogeneous' between the soft Mg matrix and reinforced carbon fibers. For metallic composites, in

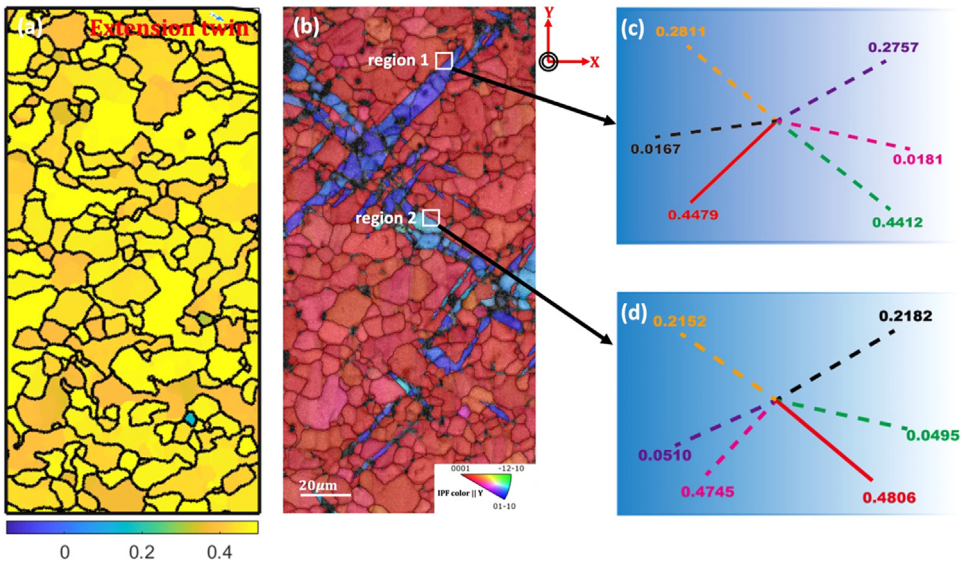

Fig. 6. (a) The recalculated max Schmid factor of extension twinning under compressive strain. (b) Two regions indicated by white squares were utilized to determine the twinning direction. (c-d) The slip traces for the possible twinning variants of parent grains in regions 1 and 2, incorporating the Schmid factor. The slip trace with the maximum Schmid factor is marked with a solid red line. (For interpretation of the references to colour in this figure legend, the reader is referred to the web version of this article.)

order to achieve compatible deformation of two phases, the geometrically necessary dislocation array will be formed at the forefront of the interface between the matrix and reinforcements, thus exerting the back stress on the matrix [42–44]. The generation of back stress, on the one hand, enables the matrix to undergo plastic deformation at higher stresses and thus exhibit higher strength, and on the other hand, promotes the occurrence of extension twinning under the overlapping of compressive residual stress in the matrix. Moreover, the vital role played by the inhomogeneous distribution of carbon fibers within the magnesium matrix cannot be overstated in the context of the remarkable phenomenon observed—namely, the activation of twinning followed by subsequent detwinning. Within the composite material exhibiting a gradient distribution of reinforcing phases along its thickness dimension, a well-established pattern of gradient structural deformation emerges. In this paradigm, plastic deformation systematically advances from a softer layer characterized by a lower density of carbon fibers to a harder layer endowed with a higher density of these fibers, as corroborated by previous research [45–47]. In the region characterized by a lower density of carbon fibers, corresponding to the soft layer, local *in-situ* observations reveal that plastic deformation initially manifests within the macroscopic elastic range. This occurrence is attributed to the confluence of compressive residual stresses within the matrix prior to deformation and compressive back stresses generated at the interface between the matrix and the reinforcing material. This convergence results in the initiation of anomalous twinning. As the extension under tension progresses, the entire specimen undergoes plastic deformation, causing the gradual dissipation of compressive residual stresses. This, in turn, allows the local stress-strain state to progressively align with the macroscopic stress-strain state, ultimately mitigating the conditions that initially sustained the anomalous extension twinning and facilitating its subsequent detwinning.

In summary, consecutive $\{10\bar{1}2\}$ extension twinning and detwinning were observed in Mg-CF composites by *in-situ* EBSD tensile test. The occurrence of anomalous twinning in the early stage of deformation was ascribed to the microscopic compressive strain, which stems from both the residual compressive stress caused by the large thermal mismatch and the back stress exerted on the matrix due to strain compatibility. This scenario, opposite to the macroscopic strain, satisfies the Schmid factor law motivating extension twins. The onset of detwinning is attributed to the gradual convergence between micro-strain and macro-strain, and the gradient distribution of CFs along the thickness dimension may be essential to capture the successive onset of twinning and detwinning. This work complements our understanding of anomalous tension twinning in magnesium alloys and magnesium-based composites.

Acknowledgments

This work was supported by Natural Science Foundation of Hunan Province Youth Fund (Grant No. 2021JJ20011), National Natural Science Foundation of China (Grant No. 52001030). H.K. Yang acknowledges the support from the International Science and Technology Cooperation Project of Guangdong Province under Grant [2022A0505050054].

Supplementary materials

Supplementary material associated with this article can be found, in the online version, at doi:10.1016/j.jma.2023.10.008.

References

[1] A.I.H. Committee, ASM int. 2 (1992) 1143–1144.
[2] C. Bettles, M. Barnett, Advances in Wrought Magnesium alloys: Fundamentals of processing, Properties and Applications, Elsevier, 2012.
[3] A. Luo, Metallur. Mater. Trans. A A 26 (1995) 2445–2455.
[4] D. Yin, C. Boehlert, L. Long, G. Huang, H. Zhou, Q. Wang, Int. J. Plasticity 136 (2021) 102878.
[5] J.W. Christian, S. Mahajan, Progress mater. sci. 39 (1–2) (1995) 1–157.
[6] M. Barnett, Mater. Sci. Eng.: A 464 (1–2) (2007) 1–7.
[7] M. Yoo, Metallur. trans. A 12 (3) (1981) 409–418.
[8] D. Shi, J. Zhang, Materials 15 (16) (2022) 5510.
[9] Y. Chai, C. Boehlert, Y. Wan, G. Huang, H. Zhou, J. Zheng, Q. Wang, D. Yin, Metallur. Mater. Trans. A 52 (2) (2021) 449–456.
[10] W. Huang, Q. Huo, Z. Xiao, Z. Fang, A. Hashimoto, X. Yang, Mater. Sci. Eng.: A 792 (2020) 139699.
[11] K. Vaishakh, N. Subrahmanya Prasad, R. Narasimhan, J. Eng. Mater. Technol. 141 (3) (2019).
[12] K.D. Molodov, T. Al-Samman, D.A. Molodov, G. Gottstein, Acta Materialia 103 (2016) 711–723.
[13] J.J. Jonas, S. Mu, T. Al-Samman, G. Gottstein, L. Jiang, Ė. Martin, Acta Materialia 59 (5) (2011) 2046–2056.
[14] J. Koike, Y. Sato, D. Ando, Mater. trans. (2008) 0811070603 -0811070603.
[15] J. Jiang, A. Godfrey, W. Liu, Q. Liu, Scripta Materialia 58 (2) (2008) 122–125.
[16] P. Yang, Y. Yu, L. Chen, W. Mao, Scripta Materialia 50 (8) (2004) 1163–1168.
[17] M.D. Nave, M.R. Barnett, Scripta Materialia 51 (9) (2004) 881–885.
[18] S. Hua, Z. Jiang, Y. Wan, G. Huang, H. Zhou, J. Zheng, Q. Wang, D. Yin, Mater. Sci. Eng.: A 825 (2021) 141927.
[19] D. Ando, J. Koike, Y. Sutou, Acta Materialia 58 (13) (2010) 4316–4324.
[20] F. Wang, S. Sandlöbes, M. Diehl, L. Sharma, F. Roters, D. Raabe, Acta materialia 80 (2014) 77–93.
[21] J. Wang, M.R.G. Ferdowsi, S.R. Kada, P.A. Lynch, Z. Wang, J.A. Kimpton, M.R. Barnett, Acta Materialia 205 (2021) 116531.
[22] X. Guo, Y. Cheng, Y. Xin, W. Wu, C. Ma, K. An, P.K. Liaw, P. Wu, Q. Liu, J. Mechan. Phys. Solids (2022) 105030.
[23] D. Xie, Z. Lyu, Y. Li, P.K. Liaw, H.B. Chew, Y. Ren, Y. Chen, K. An, Y. Gao, Mater. Sci. Eng.: A 806 (2021) 140860.
[24] F. Wang, H. Qiao, Y. Wang, J. Dong, Y. Jiang, P. Wu, Int. J. Plasticity 147 (2021) 103109.
[25] S. Dong, Q. Yu, Y. Jiang, J. Dong, F. Wang, W. Ding, Mater. Design (1980-2015) 65 (2015) 762–765.
[26] O. Muránsky, D. Carr, P. Šittner, E. Oliver, Int. J. Plasticity 25 (6) (2009) 1107–1127.
[27] L. Wu, A. Jain, D. Brown, G. Stoica, S. Agnew, B. Clausen, D. Fielden, P. Liaw, ZK60A, Acta Materialia 56 (4) (2008) 688–695.
[28] L. Wu, S. Agnew, D. Brown, G. Stoica, B. Clausen, A. Jain, D. Fielden, P. Liaw, ZK60A, Acta Materialia 56 (14) (2008) 3699–3707.
[29] A.D. Murphy-Leonard, D.C. Pagan, A. Beaudoin, M.P. Miller, J.E. Allison, Int. J. Fatigue 125 (2019) 314–323.
[30] Y. Cui, Y. Li, Z. Wang, X. Ding, Y. Koizumi, H. Bian, L. Lin, A. Chiba, nt. J. Plasticity 91 (2017) 134–159.
[31] Y.J. Wu, R. Zhu, J.T. Wang, W.Q. Ji, Scripta Materialia 63 (11) (2010) 1077–1080.
[32] W. Gong, R. Zheng, S. Harjo, T. Kawasaki, K. Aizawa, N. Tsuji, J. Magnes. Alloys (2022).
[33] J. Wang, M.R.G. Ferdowsi, S.R. Kada, C.R. Hutchinson, M.R. Barnett, Scripta Materialia 160 (2019) 5–8.
[34] M.R. Barnett, M.D. Nave, A. Ghaderi, Acta Materialia 60 (4) (2012) 1433–1443.
[35] M.A. Kumar, I.J. Beyerlein, R.J. McCabe, C.N. Tome, Nat. commun. 7 (1) (2016) 1–9.
[36] S. Godet, L. Jiang, A. Luo, J. Jonas, Scripta Materialia 55 (11) (2006) 1055–1058.
[37] D. Zhao, X. Ma, A. Srivastava, G. Turner, I. Karaman, K.Y. Xie, Acta Materialia 207 (2021) 116691.
[38] W. Hutchinson, M. Barnett, Scripta Materialia 63 (7) (2010) 737–740.
[39] G. Geng, X. Ma, H. Geng, Y. Wu, Chem. Res. Chin. Unive. 34 (3) (2018) 451–456.
[40] A. Sharma, V.M. Sharma, B. Sahoo, S.K. Pal, J. Paul, J. Manuf. Processes 37 (2019) 53–70.
[41] Z.W. Zhang, Z.Y. Liu, B.L. Xiao, D.R. Ni, Z.Y. Ma, Carbon 135 (2018) 215–223.
[42] M.F. Ashby, J. Theoret. Experiment. Appl. Phys. 21 (170) (1970) 399–424.
[43] M. Taya, Mater. Trans., JIM 32 (1) (1991) 1–19.
[44] R. Xu, G. Fan, Z. Tan, G. Ji, C. Chen, B. Beausir, D.-B. Xiong, Q. Guo, C. Guo, Z. Li, D. Zhang, Mater. Res. Lett. 6 (2) (2018) 113–120.
[45] T.H. Fang, W.L. Li, N.R. Tao, K. Lu, Science 331 (6024) (2011) 1587–1590.
[46] X. Li, L. Lu, J. Li, X. Zhang, H. Gao, Nature Rev. Mater. 5 (9) (2020) 706–723.
[47] E. Ma, T. Zhu, Mater. Today 20 (6) (2017) 323–331.

Wei Zhao[#]
Institute of Metals, College of Materials Science and Engineering, Changsha University of Science & Technology, Changsha 410114, China

Zhihao Jiang[#]
Department of Mechanical Engineering, City University of Hong Kong, Hong Kong, China

Xiang Wu
Yujing Liu
Institute of Metals, College of Materials Science and Engineering, Changsha University of Science & Technology, Changsha 410114, China

Haokun Yang[*]
Smart manufacturing division, Hong Kong Productivity Council, Hong Kong SAR 999077, China

Jun Wang[*]
Institute for Frontier Materials, Deakin University, Geelong, VIC 3216, Australia

Qi Liu
Institute of Metals, College of Materials Science and Engineering, Changsha University of Science & Technology, Changsha 410114, China
Department of Industrial and Systems Engineering, The Hong Kong Polytechnic University, Hong Kong, China

Xiaochun Liu[*]
Institute of Metals, College of Materials Science and Engineering, Changsha University of Science & Technology, Changsha 410114, China

[*]Corresponding authors.
E-mail addresses: hkyang@hkpc.org (H. Yang), jun.wang2@deakin.edu.au (J. Wang), xcliu@csust.edu.cn (X. Liu)
[#] These authors contribute equally to this work.

Received 6 April 2023
Revised 26 September 2023
Accepted 25 October 2023